

# Magnetic Field Correlation Imaging

Jens H. Jensen,<sup>1\*</sup> Ramesh Chandra,<sup>1</sup> Anita Ramani,<sup>1</sup> Hanzhang Lu,<sup>1</sup> Glyn Johnson,<sup>1</sup> Sang-Pil Lee,<sup>2</sup> Kyle Kaczynski,<sup>3</sup> and Joseph A. Helpert<sup>1,2</sup>

**A magnetic resonance imaging (MRI) method is presented for estimating the magnetic field correlation (MFC) associated with magnetic field inhomogeneities (MFIs) within biological tissues. The method utilizes asymmetric spin echoes and is based on a detailed theory for the effect of MFIs on nuclear magnetic resonance (NMR) signal decay. The validity of the method is supported with results from phantom experiments at 1.5 and 3 T, and human brain images obtained at 3 T are shown to demonstrate the method's feasibility. The preliminary results suggest that MFC imaging may be useful for the quantitative assessment of iron within the brain. Magn Reson Med 55:1350–1361, 2006. © 2006 Wiley-Liss, Inc.**

**Key words:** MRI; brain; iron; magnetic field inhomogeneities; asymmetric spin echo

The nuclear magnetic resonance (NMR) water signal obtained from a biological tissue may be strongly influenced by magnetic field inhomogeneities (MFIs) generated by spatial variations in magnetic susceptibility. These variations can be due to macroscopic structures, such as air cavities, bone, or large veins. More interestingly, there can also be microscopic MFIs, with length scales ranging roughly from 1 to 100  $\mu\text{m}$ , which are produced, for example, by capillaries, iron rich cells, or the presence of an extracellular paramagnetic contrast agent. Information about these types of microscopic magnetic tissue structures is therefore encoded in the NMR signal.

The conventional MR method for exploiting the effect of MFIs has been to measure the relaxation rates  $R_2 = 1/T_2$  or  $R_2^* = 1/T_2^*$ . This approach has, in particular, been applied to study the distribution of iron in the brain (1) and to quantify iron overload in the liver (2,3) and heart (4,5). A possible disadvantage of using these relaxation rates to assess MFIs is that they are also influenced by molecular relaxation mechanisms, such as dipole-dipole interactions. Thus  $R_2$  and  $R_2^*$  are not specific indicators of MFIs.

Some studies have also utilized the derived relaxation rate  $R_2' = R_2^* - R_2$  (6–8). Since molecular relaxation mechanisms typically increase the  $R_2$  and  $R_2^*$  by about the same amount,  $R_2'$  can provide a better characterization of MFIs than either  $R_2$  or  $R_2^*$  separately. However, the precise phys-

ical meaning of  $R_2'$  is not always apparent because of its complicated theoretical relationship to MFIs (9–15). Moreover,  $R_2'$  may sometimes be poorly defined, as NMR signal decay in the presence of MFIs may deviate significantly from a monoexponential form (9–18). Measured  $R_2'$  values will then be dependent on the experimental details.

Here we describe a new MRI method for determining a quantitative measure of MFIs, the magnetic field correlation (MFC). The MFC has a much more direct relationship to the MFIs than does  $R_2'$ , allowing for a clearer physical interpretation. In addition, MFC imaging is based on a detailed theoretical model of NMR relaxation in the presence of MFIs that includes nonmonoexponential decay effects. As a consequence, MFC imaging data may be less sensitive than  $R_2'$  to variations in experimental technique. MFC imaging was originally proposed by Jensen et al (19,20) and Helpert et al (21), but a detailed presentation of the method has not been previously published.

The main purpose of this article is to explain the theoretical basis of MFC imaging. In addition, we give results from phantom experiments to support the theory's validity. Finally, we show some human brain MFC images, primarily to demonstrate the method's feasibility for in vivo studies. This preliminary data suggests that MFC imaging may be useful for brain iron quantification, which is of interest for a variety of neuropathologies including Alzheimer's and Parkinson's diseases (22).

## THEORY

### Definition of Magnetic Field Correlation

The total magnetic field experienced by an individual water molecule at time  $t$  can be decomposed as

$$B_{\text{tot}}(t) = B_0 + B(t), \quad [1]$$

where  $B_0$  is the uniform average field and  $B(t)$  reflects the MFIs. The time dependence of  $B(t)$  is due to water diffusion. If there are significant microscopic MFIs with a length scale  $L$ , then  $B(t)$  will vary on a time scale of  $T \approx L^2/6D$ , where  $D$  is the water diffusion coefficient. For  $L = 10 \mu\text{m}$  and  $D = 1 \mu\text{m}^2/\text{ms}$ , which is a typical diffusion coefficient value for biological tissues, this yields a time scale of about 17 ms.

Now consider the temporal correlation function

$$K(|t - t'|) = \langle B(t)B(t') \rangle, \quad [2]$$

where the angle brackets indicate an averaging over all the water molecules within a voxel. This depends only on the time difference  $t - t'$  because of time translation invariance. With increasing time,  $K(t)$  will normally decrease due to the effect of diffusion. Its initial value,  $K(0)$ , is

<sup>1</sup>Center for Biomedical Imaging, Department of Radiology, New York University School of Medicine, New York, New York.

<sup>2</sup>Center for Advanced Brain Imaging, The Nathan Kline Institute, Orangeburg, New York.

<sup>3</sup>Siemens Medical Solutions USA, Parsippany, New Jersey.

Grant sponsor: National Institutes of Health (NIH); Grant number: NIH/NIBIB R21/R33 EB003305; Grant sponsor: Institute for the Study of Aging; Grant sponsor: Werner Dannheisser Testamentary Trust.

\*Correspondence to: Jens H. Jensen, Department of Radiology, New York University School of Medicine, KIP-600-A, 650 First Avenue, New York, NY 10016-3240. E-mail: jens.jensen@med.nyu.edu

Received 21 April 2005; Revised 4 January 2006; Accepted 21 February 2006. DOI 10.1002/mrm.20907

Published online 12 May 2006 in Wiley InterScience (www.interscience.wiley.com).

simply the variance for the MFIs. It should be noted that, by definition,  $\langle B(t) \rangle = 0$ .

In biological tissues,  $K(0)$  is generally less than about  $10^{-12} \text{ T}^2$ , at clinical MRI field levels of 1.0 to 3.0 T. For this reason, it is convenient to define the MFC at a time  $t$  as  $\gamma^2 K(t)$ , where  $\gamma = 2.675 \times 10^8 \text{ s}^{-1} \text{ T}^{-1}$  is the proton gyro-magnetic ratio. MFC values will then usually be in the range of 0 to  $50,000 \text{ s}^{-2}$ .

If the components of a tissue are all either diamagnetic or paramagnetic, then the MFIs will depend linearly on the applied field strength. The MFC will then grow quadratically with the applied field, as follows from Eq. [2]. However, this quadratic scaling of the MFC may not always be exact, since ferritin iron, which is a common nonheme form of iron in the human body, can be weakly superparamagnetic (23).

### Measuring the MFC with MRI

The central idea of this work is that MRI can be used to estimate the MFC in biological tissues in a simple, direct manner (19). The method is based on the weak field theory of Jensen and Chandra (13). Within this approximation, the magnitude of the NMR signal at a time  $t$  is given by

$$S(t) = S_0 \exp\left(-\frac{t}{T_2}\right) \times \exp\left[-\frac{\gamma^2}{2} \int_0^t dt_a \int_0^t dt_b \sigma(t_a) \sigma(t_b) K(|t_a - t_b|)\right], \quad [3]$$

where  $S_0$  is the initial signal intensity,  $\sigma(t_a)$  is the spin flip function, and  $T_2$  is the transverse relaxation rate in the absence of the MFIs. The spin flip function has a magnitude of unity and changes sign at the time of any  $180^\circ$  refocusing pulses, as described in detail in Ref. 13.

For the case of a single refocusing pulse at a time  $t_p$ , the spin flip function is simply

$$\sigma(t_a) = \begin{cases} -1, & \text{for } t_a < t_p < t \\ 1, & \text{otherwise.} \end{cases} \quad [4]$$

Applying Eq. [4] to Eq. [3] yields

$$S(t; t_p) = S_0 \exp\left(-\frac{t}{T_2}\right) \times \exp\left[-\frac{\gamma^2}{2} \int_0^{t_p} dt_a \int_0^{t_p} dt_b \right. \\ \times K(|t_a - t_b|) \left. \right] \times \exp\left[\gamma^2 \int_{t_p}^t dt_a \int_0^{t_p} dt_b K(|t_a - t_b|)\right] \\ \times \exp\left[-\frac{\gamma^2}{2} \int_{t_p}^t dt_a \int_{t_p}^t dt_b K(|t_a - t_b|)\right], \quad [5]$$

where it is assumed that  $t > t_p$ . Note that  $t_p = t/2$  corresponds to a symmetric spin echo (SSE) at the time  $t$  and that  $t_p \neq t/2$  corresponds to an asymmetric spin echo (ASE).

As shown in the Appendix, one may deduce from Eq. [5] that

$$\ln\left[\frac{S(t; t/2)}{S(t; t_s + t/2)}\right] = 2\gamma^2 t_s \int_{-t_s}^{t_s} ds (1 - |s/t_s|) K(s + t/2). \quad [6]$$

Physically, Eq. [6] states that the ratio of the signal intensity of an SSE acquired at a time  $t$  to an ASE acquired at the same time depends only on the MFC for times ranging from  $-t_s + t/2$  to  $t_s + t/2$ . If the pulse time shift  $t_s$  is not too large, then it is reasonable to utilize the Taylor expansion  $K(s + t/2) = K(t/2) + sK'(t/2) + O(s^2)$  in the integral of Eq. [6], which gives

$$\ln\left[\frac{S(t; t/2)}{S(t; t_s + t/2)}\right] = 2\gamma^2 t_s^2 K(t/2) + O(t_s^4). \quad [7]$$

Hence for small  $t_s$ , the SSE to ASE signal intensity ratio can be used to determine the MFC at the spin echo refocusing pulse time of  $t/2$ .

Equation [7] implies

$$S(t; t_s + t/2) \approx S(t; t/2) \exp[-2\gamma^2 t_s^2 K(t/2)], \quad [8]$$

so that the ASE signal intensity is approximately a Gaussian function in the refocusing pulse time shift  $t_s$ . In practice, it is by fitting MRI data to Eq. [8] that MFC estimates are obtained. Note that Eq. [8] does not depend on the  $T_2$  relaxation time.

Following a similar derivation, the single spin echo formula of Eq. [6] can be generalized to multiple spin echo sequences as

$$\ln\left[\frac{S_n(0)S_{n-1}(t_s)}{S_n(t_s)S_{n-1}(0)}\right] \\ = (-1)^{n+1} 2\gamma^2 t_s \int_{-t_s}^{t_s} ds (1 - |s/t_s|) K[s + (2n-1)\Delta t], \quad [9]$$

where  $2\Delta t$  is the interecho time and  $S_n(t_s)$  is the signal intensity of the  $n$ th echo. The  $n$ th echo is acquired at the time  $2n\Delta t$ , and  $t_s$  indicates the shift of the refocusing pulses from their usual times of  $(2n-1)t$ . All the refocusing pulses must be shifted by the same amount. Adopting the convention  $S_0(t_s) \equiv S_0$ , Eq. [9] reduces to Eq. [6] for  $n = 1$ . In analogy with Eq. [8], Eq. [9] implies the approximation

$$\frac{S_n(t_s)}{S_{n-1}(t_s)} \approx \frac{S_n(0)}{S_{n-1}(0)} \exp\{(-1)^n 2\gamma^2 t_s^2 K[(2n-1)\Delta t]\}. \quad [10]$$

The anomalous sign in the exponent for even  $n$ , reflects an enhanced refocusing for even order echoes as compared to odd order echoes. By fitting Eq. [10] to multiple spin echo data, the MFC at several different times can be acquired in parallel. A disadvantage, however, of a multiple spin echo approach is the possibility of confounding effects due to refocusing pulse imperfections.

### Validity

In deriving the basic result of Eq. [8] (or Eq. [10]), essentially two key assumptions have been made: Condition 1, that the weak field theory is valid; and Condition 2, that  $t_s$  is short enough to justify the Taylor expansion used to obtain Eq. [7]. Condition 2 can always be satisfied, since the pulse time shift can be chosen to be arbitrarily small. However, MFC estimates made with too small  $t_s$  values may have large statistical uncertainties due to noise. If we assume that the MFIs scale with the applied field (which is generally the case), then Condition 1 can also be guaranteed, in principle, by reducing the field level.

Although our derivation of Eq. [8] has made use of the weak field theory, its validity is not restricted to the weak field regime. In particular, in the absence of diffusion, Eq. [8] can be shown to be exact (in the limit of small  $t_s$ ). To see this, we first note, following the formalism of Jensen and Chandra (13), that without diffusion

$$S(t) = S_0 \exp\left(-\frac{t}{T_2}\right) \times \left| \exp\left[-i\gamma B(0) \int_0^t dt_a \sigma(t_a)\right] \right|. \quad [11]$$

By taking the spin flip function for a single refocusing pulse of Eq. [4], Eq. [11] reduces to

$$S(t; t_p) = S_0 \exp\left(-\frac{t}{T_2}\right) \times |\exp[-i\gamma(t - 2t_p) B(0)]|, \quad [12]$$

provided  $t > t_p$ . The logarithm of the SSE to ASE signal intensity ratio is then seen to be

$$\ln\left[\frac{S(t; t/2)}{S(t; t_s + t/2)}\right] = -\ln\{|\exp[2i\gamma t_s B(0)]|\}. \quad [13]$$

Expanding this in powers of  $t_s$  yields

$$\ln\left[\frac{S(t; t/2)}{S(t; t_s + t/2)}\right] = 2\gamma^2 t_s^2 K(0) + O(t_s^4). \quad [14]$$

This is identical to Eq. [7] when diffusion effects are neglected, which shows that Eq. [8] holds in this case. The main criterion for the validity of the expansion of Eq. [14] is that

$$2\gamma^2 t_s^2 K(0) \ll 1. \quad [15]$$

It is plausible, if not rigorously justified, to take the natural generalization of Eq. [15],

$$2\gamma^2 t_s^2 K(t/2) \ll 1, \quad [16]$$

as a basic condition for the applicability of Eq. [8]. Equation [15], as well as the generalization of Eq. [16], may be readily extended to the multiple spin echo formula of Eq. [10].

While Eq. [16] provides a rough guideline for the validity of the MFC imaging method, it can be difficult to determine a priori whether Eq. [8] holds for a particular

experimental arrangement. However, numerical evidence based on Monte Carlo simulations indicates this may well be the case for biological tissues at clinical field levels (19). In practice, it is convenient to take the viewpoint that a fit to Eq. [8] defines an “apparent” MFC much as a monoexponential fit to the signal intensity versus  $b$ -value data is used to define an apparent diffusion coefficient in diffusion-weighted MRI. The apparent MFC can then be regarded as an approximation to the true MFC, with the understanding that the nature of this approximation may at times be subtle.

An implicit assumption we have made is that the  $T_2$  relaxation rate, in the absence of the MFIs, is the same throughout the voxel. This implies that partial volume effects could alter measured MFC values. In addition, the presence of fat is a potential confounding factor, since the significant resonant frequency difference between fat and water can strongly affect ASE signal intensities. Indeed, one of the original applications of ASEs is to separate fat and water signals (24).

Of course, any MRI acquisition requires the imposition of imaging gradients. These are assumed to have a negligible effect on measured MFC values. Another practical consideration is that the receiver bandwidth be large enough to afford a sufficient temporal resolution. More specifically, the bandwidth/pixel should be much greater than  $(\text{MFC})^{1/2}$ .

### Special Cases

To appreciate the physical significance of MFC imaging data, it is instructive to cite some established approximations for  $K(t)$ , such as those that have been discussed in detail by Jensen and Chandra (13). Perhaps the most commonly used approximation is

$$K(t) = K(0)e^{-t/\tau}, \quad [17]$$

where  $\tau$  is a characteristic decay time (25). Alternatively, for unrestricted water diffusion, Jensen and Chandra (13) have argued that a more accurate functional form is given by

$$K(t) = K(0) \left(1 + \frac{4Dt}{r_c^2}\right)^{-3/2}, \quad [18]$$

where  $r_c$  is a characteristic length for the MFIs. This implies that the MFC will decrease to half its initial value in a time  $t \approx r_c^2/(6.81 \cdot D)$ , which is nearly the same as the mean time for a water molecule to diffuse a distance  $r_c$ .

For the particular model of MFIs generated by randomly distributed, identical penetrable spheres of radius  $R$ , one has the exact expression (13)

$$K(t) = \frac{256\pi^3}{135} \rho R^3 \chi^2 B_0^2 U\left(\frac{Dt}{R^2}\right), \quad [19]$$

where  $\rho$  is the number of spheres per unit volume and  $\chi$  is the magnetic susceptibility difference between the spheres and the surrounding media. The function  $U$  is given by

$$U(x) = \frac{1}{\sqrt{\pi}} \left\{ \sqrt{\pi} \Phi \left( \frac{1}{\sqrt{x}} \right) + 2x^{3/2} [1 - e^{-1/x}] - x^{1/2} [3 - e^{-1/x}] \right\}, \quad [20]$$

where  $\Phi(x)$  is the probability integral. In this case,  $K(t) = K(0)/2$  for  $t \approx R^2/(10 \cdot D)$ .

### Macroscopic Gradients

Microscopic magnetic susceptibility variations within a voxel are often the main source of its MFIs. However, macroscopic susceptibility variations, produced for example by air cavities or large veins, can generate field gradients that affect many nearby voxels. To understand how such macroscopic gradients alter MFC values, it is helpful to formally separate the macroscopic and microscopic contributions to the MFC.

The gradient field,  $\mathbf{G}$ , within a voxel is determined by the condition

$$\langle B(t)[\mathbf{r}(t) - \mathbf{r}_0] \rangle = \langle \mathbf{G} \cdot [\mathbf{r}(t) - \mathbf{r}_0] [\mathbf{r}(t) - \mathbf{r}_0] \rangle, \quad [21]$$

with  $\mathbf{r}_0 = \langle \mathbf{r}(t) \rangle$  representing the position of the voxel's center. Observe that  $\mathbf{G}$  is independent of  $t$  due to time translation invariance (a small effect of water molecules leaving and entering the voxel is neglected). If we assume the voxel is a rectangular parallelepiped with edges of lengths  $L_x$ ,  $L_y$ , and  $L_z$  oriented parallel to the  $x$ ,  $y$ , and  $z$  Cartesian coordinate axes, then the components of  $\mathbf{G}$  are

$$\begin{aligned} G_x &= \frac{12}{L_x^2} \langle B(t)[x(t) - x_0] \rangle, \\ G_y &= \frac{12}{L_y^2} \langle B(t)[y(t) - y_0] \rangle, \\ G_z &= \frac{12}{L_z^2} \langle B(t)[z(t) - z_0] \rangle, \end{aligned} \quad [22]$$

where we have used the conventional component notations defined by  $\mathbf{r} = (x, y, z)$  and  $\mathbf{r}_0 = (x_0, y_0, z_0)$ .

From Eq. [21], one may show that the MFIs can be decomposed as

$$B(t) = B_{\text{micro}}(t) + \mathbf{G} \cdot [\mathbf{r}(t) - \mathbf{r}_0], \quad [23]$$

with the microscopic contribution satisfying the conditions

$$\begin{aligned} \langle B_{\text{micro}}(t) \rangle &= 0, \\ \langle B_{\text{micro}}(t)[\mathbf{r}(t) - \mathbf{r}_0] \rangle &= 0. \end{aligned} \quad [24]$$

From Eqs. [2] and [22–24], we then find

$$\begin{aligned} K(|t - t'|) &= \langle B_{\text{micro}}(t) B_{\text{micro}}(t') \rangle + \frac{1}{12} (G_x^2 L_x^2 + G_y^2 L_y^2 + G_z^2 L_z^2) \\ &\quad - \langle [B_{\text{micro}}(t) - B_{\text{micro}}(t')] [\mathbf{G} \cdot [\mathbf{r}(t) - \mathbf{r}(t')]] \rangle \\ &\quad - \frac{1}{2} \langle \{\mathbf{G} \cdot [\mathbf{r}(t) - \mathbf{r}(t')]\}^2 \rangle. \end{aligned} \quad [25]$$

The last term on the right hand side of Eq. [25] has the order of magnitude  $D|t - t'| \cdot |\mathbf{G}|^2$ , which is much smaller than the second term provided the diffusion length,  $(6D|t - t'|)^{1/2}$ , is small compared to the voxel dimensions. This will almost always be the case in practice, since MRI experiments probe diffusion on time scales of no more than about 200 ms, corresponding to a diffusion length of about 35  $\mu\text{m}$ .

The third term on the right hand side of Eq. [25] represents the cross correlation of the microscopic MFIs with the macroscopic gradients. On physical grounds, it is reasonable to suppose that this term is small, since the sources of the macroscopic gradients are largely from outside the voxel and typically independent of the microscopic MFIs which are due primarily to intravoxel magnetic susceptibility variations. More rigorously, we have the inequality

$$|\langle [B_{\text{micro}}(t) - B_{\text{micro}}(t')] [\mathbf{G} \cdot [\mathbf{r}(t) - \mathbf{r}(t')]] \rangle| < K(0), \quad [26]$$

which is demonstrated in the Appendix. Thus the cross correlation can, at worst, become significant only on time scales for which the MFC has decreased substantially below its initial value.

The above considerations support the approximation

$$K(t) \approx K_{\text{micro}}(t) + \frac{1}{12} (G_x^2 L_x^2 + G_y^2 L_y^2 + G_z^2 L_z^2), \quad [27]$$

where  $K_{\text{micro}}(|t - t'|) = \langle B_{\text{micro}}(t) B_{\text{micro}}(t') \rangle$ . Hence the MFC can be regarded as the sum of microscopic and macroscopic contributions, which differ in important respects. The microscopic contribution depends on time, but is independent (or weakly dependent) on the voxel size. In contrast, the macroscopic contribution is time independent, but depends quadratically on the voxel dimensions.

Since it is the microscopic component of the MFC that is usually of interest, it is advantageous to image with the smallest voxel size that gives an adequate signal-to-noise ratio (SNR), in order minimize the effect of any macroscopic gradients. In addition, isotropic voxels are preferable both for minimizing the macroscopic gradient contribution for a given SNR and for minimizing the dependence of the MFC on the voxel's spatial orientation.

Equation [27] implies that the difference between the MFC obtained at two different times is independent of the macroscopic gradients. Such a differential MFC value can be deduced from MFC estimates based on two separate single spin echo experiments. Alternatively, one can use a dual spin echo sequence to derive an MFC difference more directly. From Eq. [10], one can show that

$$S_2(t_s) \approx S_2(0) \exp\{-2\gamma^2 t_s^2 [K(\Delta t) - K(3\Delta t)]\}, \quad [28]$$

Therefore, the use of dual spin echoes may be advantageous under circumstances with large macroscopic gradients. More generally, one may show that the signal intensity of all the even order echoes described by Eq. [10] are independent of the macroscopic gradients.



### Connection to Carr-Purcell-Meiboom-Gill $R_2$ Values

Microscopic MFIs in both the brain and blood have been previously investigated by measuring the dependence of  $R_2$ , as measured with a Carr-Purcell-Meiboom-Gill (CPMG) sequence, on the interecho time (13,26–30). Because of the combined effects of MFIs and water diffusion,  $R_2$  is observed to increase as the interecho time is lengthened.

Within the weak field approximation, the relationship between the MFC and  $R_2$  as measured with a CPMG sequence is (13)

$$R_2 = R_{2,0} + \frac{8}{\pi^2} \sum_{m=0}^{\infty} \frac{1}{(2m+1)^2} \int_0^{\infty} dt \gamma^2 K(t) \cos\left[\frac{(2m+1)\pi t}{2\Delta t}\right], \quad [29]$$

where  $R_{2,0}$  is the transverse relaxation rate in the absence of the MFIs and  $2\Delta t$  is the interecho time. Thus the interecho time dependence of  $R_2$  also provides information about the MFC. However, as Eq. [29] implies, the connection between  $R_2$  and the MFC is mathematically complex, and it would be difficult to obtain model independent values for the MFC at a specific time using only  $R_2$  data. Our MFC imaging procedure, in contrast, yields MFC estimates in a straightforward manner.

## METHODS

### Phantom Study

A phantom was constructed from six 60-ml plastic bottles. One bottle was filled with a mixture of water and Sephadex (G-25 Superfine; Amersham Biosciences, Uppsala, Sweden). Sephadex consists of particles of cross-linked dextran with a wet bead size range of 17 to 70  $\mu\text{m}$  for the grade employed. Since water and dextran have different magnetic susceptibilities, microscopic MFIs could then be expected in the Sephadex bottle when placed in a strong magnetic field. A second bottle contained water doped with a small amount of gadopentetate dimeglumine (Gd-DTPA) in order to shorten  $T_1$ . The remaining bottles were filled with corn syrup and were included to mechanically stabilize the other two. Corn syrup was used because of its extremely short  $T_2$ , which effectively eliminates the signal from these bottles in  $T_2$ -weighted images and thereby reduces imaging artifacts. The six bottles were attached with a rubber band, placed in a plastic container, and surrounded with a corn syrup bath. The corn syrup bath served to reduce macroscopic MFIs within the bottles.

The phantom was first imaged at room temperature with a Siemens 3-T Trio MRI scanner. A segmented echo planar imaging (EPI) ASE sequence was used with an EPI factor of 37. EPI was chosen to be consistent with the human study, for which EPI is critical in reducing both motion artifacts and the acquisition time. The field of view (FOV) was  $256 \times 256 \text{ mm}^2$ , the acquisition matrix size was  $128 \times 128$ , and the slice thickness was 2 mm, resulting in isotropic  $2\text{-mm}^3$  voxels. The bandwidth was 1345 Hz/pixel, and the repetition time (TR) was 2 s. Images for a single slice were obtained at echo times (TE) of 40, 50, 60, 80, and 100 ms. For each TE, images were acquired with refocusing pulse

time shifts of  $t_s = 0, -4, -8, -12$ , and  $-15$  ms, where the negative sign indicates a reduction of the interval between the initial  $90^\circ$  excitation pulse and  $180^\circ$  refocusing pulse from the SSE value of  $\text{TE}/2$ . (Note: TE is the acquisition time for the images and should not be confused with the spin echo refocusing time of  $\text{TE} + 2t_s$ .) For each set of imaging parameters, 20 images were obtained and averaged to increase the SNR. In order to test the field dependence of the MFC, the phantom was subsequently imaged with a Siemens 1.5-T Avanto MRI scanner using an identical imaging protocol.

In addition to the ASE images needed for the determination of the MFC, the phantom was scanned at 3 T with a proton-density-weighted sequence, in order to estimate the water content of the Sephadex bottle, and with a diffusion-weighted sequence, in order to estimate the diffusion coefficient. Both the proton-density-weighted and diffusion-weighted sequences had the same FOV and resolution as the ASE sequence. Other imaging parameters for the proton-density-weighted sequence were  $\text{TE} = 5$  ms,  $\text{TR} = 1.5$  s, and flip angle  $= 10^\circ$ . For the diffusion-weighted sequence, the other imaging parameters were  $\text{TE} = 91$  ms,  $\text{TR} = 2$  s, and  $b$  values of 0 and  $1000 \text{ s/mm}^2$ . The diffusion sensitizing gradients were applied in three orthogonal directions so that the trace of the diffusion tensor could be calculated.

The mean signal intensities in the water and Sephadex bottles were estimated for each image by averaging  $12 \times 12$  pixel square regions of interest (ROIs). The signal intensities for the ASE images were fit to the equation

$$S(\text{TE}; t_s + \text{TE}/2) = [\eta^2 + a_1^2 \exp(-4a_2 t_s^2)]^{1/2}, \quad [30]$$

with a separate fit being performed for each TE. The parameter  $\eta$  reflects the background noise level and was estimated from the signal intensity in air. The two fitting parameters,  $a_1$  and  $a_2$ , were determined by  $\chi^2$  minimization using the Levenberg-Marquardt method (31).

In the absence of background noise ( $\eta = 0$ ), fitting to Eq. [30] is equivalent to fitting to Eq. [8]. The modification of Eq. [30] is a conventional method for approximately including the effects of noise for MRI magnitude images (32). By comparing Eqs. [8] and [30], it is seen that the parameter  $a_2$  provides an estimate for the MFC. MFC maps for the phantom were constructed in an analogous manner by fitting the images on a pixel by pixel basis to Eq. [30].

To estimate the water content of the Sephadex bottle, the signal intensity in the proton-density-weighted images for this bottle was divided by that of the water bottle. The diffusion coefficient in the Sephadex bottle was determined from the trace of the diffusion tensor (i.e., the average of the apparent diffusion coefficient in the three orthogonal directions). This is not to imply that the diffusion was anisotropic; in fact the measured apparent diffusion coefficient was nearly the same in each direction.

### Human Study

Our human study was performed on the same 3-T scanner and with the same segmented EPI ASE sequence as for the phantom study and was approved by the New York University School of Medicine institutional review board. The

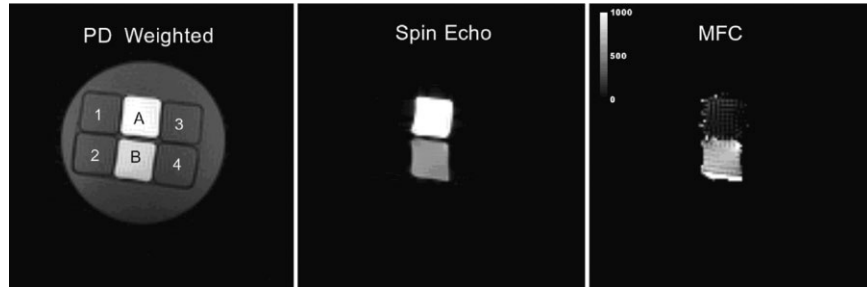


FIG. 1. Proton-density-weighted image, SSE image (labeled “spin echo”), and MFC map for the phantom obtained at 3 T. Bottles 1 through 4 are filled with corn syrup and are included merely to stabilize bottles A and B. Bottle A is filled with water, while bottle B has a mixture of water and Sephadex. Bottles 1 through 4, as well as the surrounding corn syrup bath, are not visible in the SSE image and the MFC map due to the short  $T_2$  relaxation time for corn syrup. Bottle B appears hyperintense in the MFC map because of the MFIs generated by the Sephadex. The SSE image and the MFC map were both obtained at  $TE = 40$  ms. The scale bar in the MFC map gives the MFC values in  $s^{-2}$ .

EPI factor and the TR were the same as for the phantom study, but the refocusing pulse time shifts were  $t_s = 0, -4, -8, -12$ , and  $-16$  ms. In addition, the FOV was  $220 \times 220$  mm<sup>2</sup>, the slice thickness was 1.1 mm, and the bandwidth was 1185 Hz/pixel. The slices were oriented axially with a slight tilt to avoid coming too close to the sinus cavity, which is a potential source of macroscopic MFIs. Fat saturation pulses were used to suppress the fat signal.

In a first scanning session, images were obtained with TE values of 42 ms and 70 ms and with an acquisition matrix size of  $192 \times 192$ . The entire protocol was run twice, as a test of reproducibility. The data for these two trials were analyzed separately. In a second scanning session, images were obtained with a TE of 42 ms and acquisition matrices of  $192 \times 192$ ,  $128 \times 128$ , and  $64 \times 64$ , to test the effect of resolution on the MFC values. As indicated by Eq. [27], a component of the MFC due to macroscopic gradients oriented in the image plane would be expected to increase quadratically with the voxel dimensions.

The acquisition of each set of imaging parameters was preformed 10 times. Image repetitions were coregistered and averaged to improve the SNR. The averaged images for a given slice but different refocusing pulse time shifts were also coregistered, prior to the MFC analysis. This coregistration procedure was employed to minimize motion artifacts in the MFC maps.

The ROI analysis and the MFC maps were performed in the same way as for the phantom study, except that the ROIs were chosen in the putamen. The putamen was selected because it is a large structure with a high iron concentration. The adjacent globus pallidus also has high iron content, but was less suitable for this study because the SNR is significantly lower in this region. From the pair of SSE images (i.e.,  $t_s = 0$ ) with TE = 42 ms and 70 ms,  $R_2$  maps were computed from the formula

$$R_2 = \frac{1}{TE_2 - TE_1} \cdot \ln \left[ \frac{S(TE_1; TE_1/2)}{S(TE_2; TE_2/2)} \right], \quad [31]$$

where  $TE_1 = 42$  ms and  $TE_2 = 70$  ms.

## RESULTS

### Phantom Study

The phantom arrangement is demonstrated in the proton-density-weighted image of Fig. 1. Bottles 1–4 contain corn syrup and are hypointense both because of their low water content and their extremely short  $T_2$  relaxation times. The ratio of the signal intensities of the water bottle (Fig. 1, A) to the Sephadex bottle (Fig. 1, B) indicates a water fraction of  $0.820 \pm 0.003$  in bottle B. The 3-T SSE image of Fig. 1 was obtained from the ASE sequence with TE = 40 ms and  $t_s = 0$ . Only bottles A and B are visible because of the rapid transverse relaxation of the signal in bottles 1–4 and in the surrounding corn syrup bath.

The 3-T MFC map for  $t = TE/2 = 20$  ms is also shown in Fig. 1. The MFC of the Sephadex bottle is much larger than that of the water bottle, which is consistent with the presence of microscopic MFIs in the Sephadex bottle. A small MFC is also observed in the water bottle, possibly reflecting a macroscopic gradient. The MFC maps for longer times look similar, except for a marked decrease of the MFC in the Sephadex bottle with increasing time.

Fits of the 3-T signal intensity vs. the refocusing pulse shift are illustrated in Fig. 2 for TE = 40 ms and TE = 50 ms. A good fit to Eq. [30] is seen in both cases, and fits of similar quality were obtained for the other TE values. The goodness-of-fit was quantified by the confidence level for the  $\chi^2$ . This confidence level,  $Q$ , is given by

$$Q = \frac{\Gamma(\nu/2, \chi^2/2)}{\Gamma_{(a,x)}(\nu/2, 0)}, \quad [32]$$

where  $\nu$  is the number of degrees of freedom and  $\Gamma(a, x)$  is the incomplete gamma function. The number of degrees of freedom  $\nu$  is the number of data points minus the number of fitting parameters. If all the  $t_s$  values are used, then  $\nu = 5 - 2 = 3$ , for our case. A confidence level of 0.50 or 50% means that there is a 50% chance of obtaining a  $\chi^2$  of this magnitude or larger, assuming the theoretical model is accurate (31). Confidence levels exceeding 5% are usually regarded as indicating an acceptable fit. This threshold is well surpassed for each value of TE, supporting the valid-

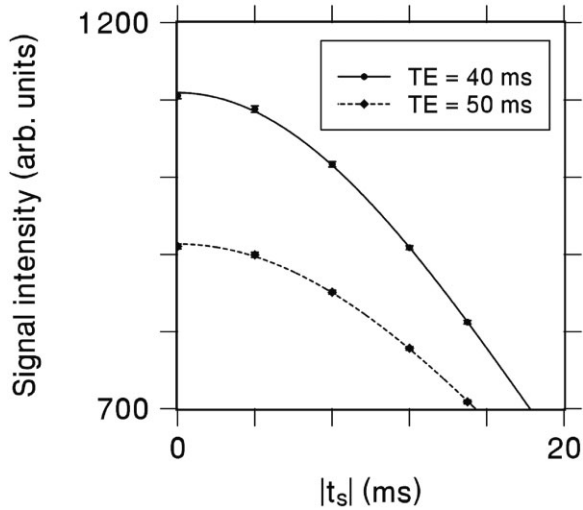


FIG. 2. Signal intensity at 3 T vs. the refocusing pulse shift in the phantom's Sephadex bottle B for TE = 40 and 50 ms. The error bars for the data points indicate standard error estimates. The lines are fits to the theoretical form of Eq. [30] using the data points with  $|t_s| \leq 15$  ms. For TE = 40 ms,  $\chi^2 = 1.63$ , corresponding to a confidence level of 65%, and for TE = 50 ms,  $\chi^2 = 1.90$ , corresponding to a confidence level of 59%.

ity of Eq. [8]. For every TE, the highest confidence level was obtained by using all five  $t_s$  values.

Both the 1.5-T and 3-T MFC values vs. time for the Sephadex and water bottles are shown in Fig. 3. In the Sephadex bottle, the MFC is seen to decrease monotonically with time, which is the theoretically expected behavior when microscopic MFIs are present. At 1.5 T, the MFC in the water bottle is zero within the experimental uncertainties. A small, time-independent MFC is observed in the water bottle at 3 T, consistent with the presence of a macroscopic gradient. The microscopic MFIs should, of course, be nearly zero in the water bottle. The macroscopic gradients within the ROIs could potentially have been affected by both the slice location and phantom placement, and thus the macroscopic contributions to the MFC for the 1.5 T and 3 T scans may not be well correlated.

The time dependence of the microscopic MFC in the Sephadex bottle can reasonably be expected to approximately follow Eq. [18]. As suggested by Eq. [27], any macroscopic gradients contribute a constant offset. Therefore the total MFC should be given by

$$\gamma^2 K(t) = C + B_0^2 \cdot \frac{\gamma^2 K_{\text{micro}}(0)}{B_0^2} \cdot \left(1 + \frac{4Dt}{r_c^2}\right)^{-3/2}, \quad [33]$$

where  $C$  is the macroscopic gradient offset. Because Sephadex is diamagnetic, the ratio  $\gamma^2 K_{\text{micro}}(0)/B_0^2$  is independent of the applied field strength. The lines in Fig. 3 are global fits of Eq. [33] to the measured MFC data. The fitting parameters  $\gamma^2 K(0)/B_0^2$  and  $4Dt/r_c^2$  were constrained to be the same for both the 1.5-T and 3-T data sets, but the macroscopic gradient offset was allowed to differ for the two field levels. In carrying out the fits, the precise applied field strengths of  $B_0 = 1.4944$  T and 2.8936 T were used. The resulting fitting parameters are

$$\gamma^2 K_{\text{micro}}(0)/B_0^2 = 532 \pm 211 \text{ s}^{-2},$$

$$\frac{4D}{r_c^2} = 0.121 \pm 0.051 \text{ ms}^{-1},$$

$$C = 19 \pm 21 \text{ s}^{-2}, \text{ for } 1.5 \text{ T},$$

$$C = 0 \pm 44 \text{ s}^{-2}, \text{ for } 3 \text{ T}. \quad [34]$$

If these estimated  $C$  values are subtracted from the measured MFC values, then the ratios of the microscopic components of the MFC for 3 T and 1.5 T are found to be 3.76, 3.71, 3.44, 4.03, and 2.81 for  $t = 20, 25, 30, 40$ , and 50 ms, respectively. These ratios are comparable the exact square field ratio of  $(2.8936/1.4944)^2 = 3.75$ , in agreement with theory.

The water diffusion coefficient in the Sephadex bottle was measured to be  $1.29 \pm 0.01 \mu\text{m}^2/\text{ms}$ . This combined with Eq. [34] then gives  $r_c = 6.5 \pm 1.4 \mu\text{m}$  for the characteristic length of the MFIs, which is comparable to the size (17  $\mu\text{m}$ ) of the smaller of the Sephadex particles. We note that for the random sphere model considered by Jensen and Chandra (13),  $r_c$  is about half the sphere diameter.

Accepting Eq. [19] as a rough approximation for the microscopic component of the MFC, we can also estimate the susceptibility difference  $\chi$  between Sephadex and water. Since  $U(0) = 1$ , Eq. [19] gives

$$\gamma^2 K_{\text{micro}}(0)/B_0^2 = \frac{256\pi^3}{135} \rho R^3 \gamma^2 \chi^2. \quad [35]$$

Equating the measured water fraction of  $0.820 \pm 0.003$  with  $1 - 4\pi\rho R^3/3$  then yields  $\chi \approx 5.4 \times 10^{-8}$ . This is not far from the range of susceptibility difference values, 0.7 to

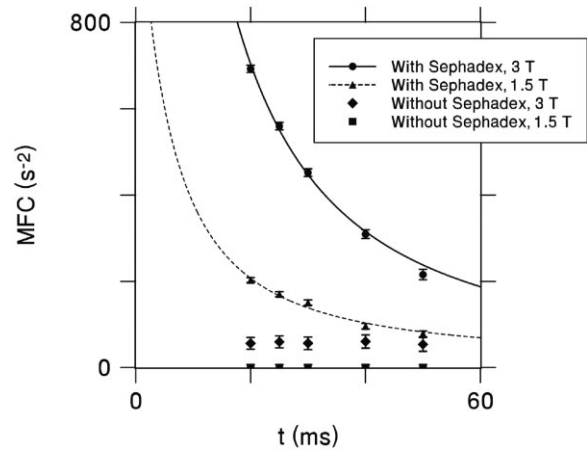
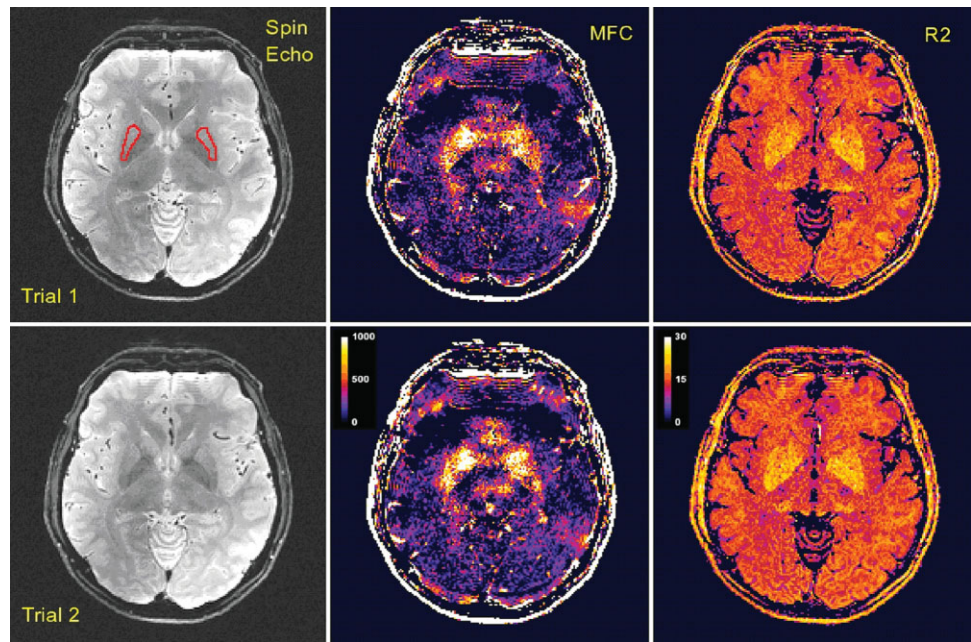


FIG. 3. MFC values in phantom bottles A (■, ◆) and B (▲, ●) vs. time obtained at both 1.5 and 3 T. The MFC in the water bottle A is small and independent of time. In the Sephadex bottle B, the MFC is much larger and varies strongly with time, which is consistent with the presence of significant microscopic MFIs. The lines are from a global fitting based on the functional form given by Eq. [33]. Note that  $t = \text{TE}/2$ , where TE is the echo time of the images used to calculate the MFC values. The error bars indicate standard error estimates.



FIG. 4. Brain images for one human subject obtained in a single scanning session. The full imaging protocol was performed twice to test reproducibility. The SSE images and MFC maps were acquired with  $TE = 42$  ms, while the  $R_2$  maps were derived from the  $TE = 42$  ms and  $TE = 70$  ms SSE images. The hyperintense regions in the centers of both the MFC and  $R_2$  maps correspond to the putamen and globus pallidus. Their large MFC and  $R_2$  values most likely reflect their high iron content. The scale bar for the MFC maps gives the MFC values in  $s^{-2}$ , and the scale bar for the  $R_2$  maps give the  $R_2$  values in  $s^{-1}$ . The putamen is outlined in the first SSE image. This region of interest was used for the quantitative analysis summarized by Figs. 5 and 6.



$1.1 \times 10^{-8}$ , measured by Kuznetsov et al (33) for starch grains, which are chemically similar to Sephadex.

#### Human Study

The anatomy of the analyzed slice for the first scanning session is shown in the  $TE = 42$  ms SSE images appearing in Fig. 4. The ROI indicated in the Trial 1 image indicates the putamen, which was selected for the quantitative analysis; a similar ROI was identified in the Trial 2 image. Fits of the signal intensity versus the refocusing pulse time shift are given in Fig. 5. The confidence levels are maximized when the data points for  $|t_s| = 16$  ms are excluded, in which case the confidence levels are consistent with a good fit. This suggests that the form of Eq. [30] is appropriate up to  $|t_s| \leq 12$  ms, but may become less accurate for larger shifts.

The MFC maps shown in Fig. 4 were calculated using just the refocusing pulse shifts with  $|t_s| \leq 12$  ms, as these gave the best fit in the putamen. The large hyperintense regions near the center of the image correspond to the putamen and globus pallidus. It is reasonable that these would have a large MFC due to the high iron concentration in these structures (34). Smaller focal bright features, presumably blood veins, are also apparent. Blood veins can generate high MFC values due to the large paramagnetic susceptibility of deoxyhemoglobin. The elevated MFC values seen in the scalp and near the brain perimeter are likely due to macroscopic gradients or EPI-related artifacts. The slight differences between the first and second trials may be attributed to motion and noise. The corresponding  $R_2$  maps, appearing in Fig. 4, are also hyperintense in the putamen and globus pallidus. However, the contrast between these two basal ganglia structures and the surrounding tissue is not as great as for the MFC maps. For example, the contrast-to-noise ratio between the putamen and frontal white matter in the MFC maps is about 2.4, while it is 1.1 for the  $R_2$  maps.

The MFC values for the two trials for both  $t = TE/2 = 21$  ms and  $t = TE/2 = 35$  ms are shown in Fig. 6. The statistical error in the MFC estimates is about 10%. The MFC drop from 21 to 35 ms is also about 10%. This is consistent with the theoretical expectations, but is not statistically significant.

SSE images and MFC maps obtained in the second scanning session for three different resolutions are shown in

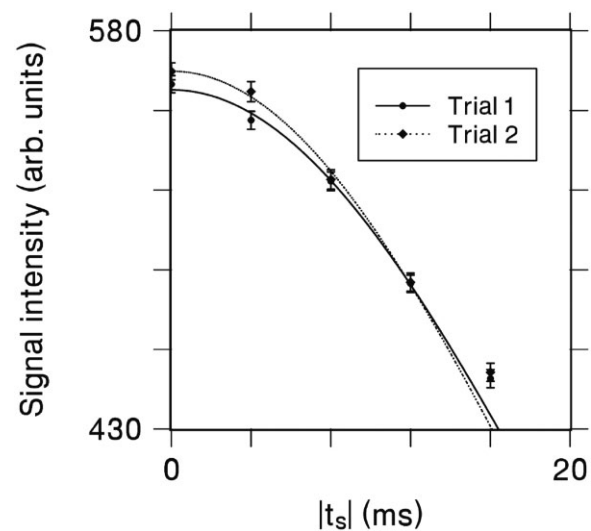


FIG. 5. Signal intensity vs. the refocusing pulse shift in the putamen for  $TE = 42$  ms. The error bars for the data points indicate standard error estimates. The lines are fits to the theoretical form of Eq. [30] using the data points with  $|t_s| \leq 12$  ms, since inclusion of the  $|t_s| = 16$  ms data points reduces the quality of the fits. For trial 1,  $\chi^2 = 1.07$ , corresponding to a confidence level of 59%, and for trial 2,  $\chi^2 = 1.12$ , corresponding to a confidence level of 57%. The data points for the two trials nearly coincide for  $|t_s| = 8$  ms and  $|t_s| = 12$  ms.



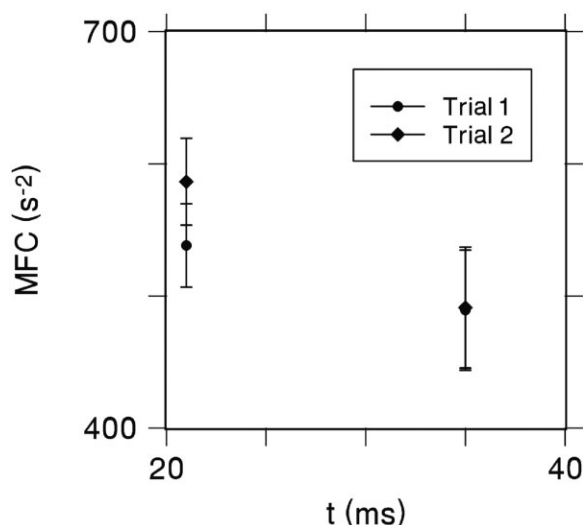


FIG. 6. MFC values in the putamen vs. time. A trend toward a decreasing MFC with time is apparent, although not statistically significant. For  $t = 35$  ms, the data points for the first and second trials nearly coincide. The error bars are standard error estimates.

Fig. 7. The data for the three resolutions were obtained serially, and the resolutions shown in Fig. 7 correspond to the acquisition matrix of the raw data. The slice position is approximately the same for each resolution, but slight differences due to movement are visible. Also shown in Fig. 7 are histograms for the MFC maps. The histograms include only values that are  $>0$  and  $<1000 \text{ s}^{-2}$  in order to exclude the background and values associated with the scalp and large vessels. The similarity of the three histograms suggests that there is little contribution to the MFC values from macroscopic gradients parallel to the image plane. As follows from Eq. [27], an effect of macroscopic gradients would result in a quadratic increase of the MFC with the voxel dimensions.

## DISCUSSION

The central idea of this article is that the MFC can be estimated by fitting ASE data to the Gaussian form of Eq. [8], for single-spin echoes, or Eq. [10] for multiple-spin echoes. Of course, ASEs have long been used in MRI (24), and the use of Gaussian fits has been previously introduced for both empirical (16,35,36) and theoretical reasons (37,38). Here, however, we have given the first detailed, rigorous derivation of a relationship between MFIs and the MFC that includes the effect of diffusion through microscopic MFIs.

A related but distinct imaging method has been previously proposed by Ma and Wehrli (7). This method,

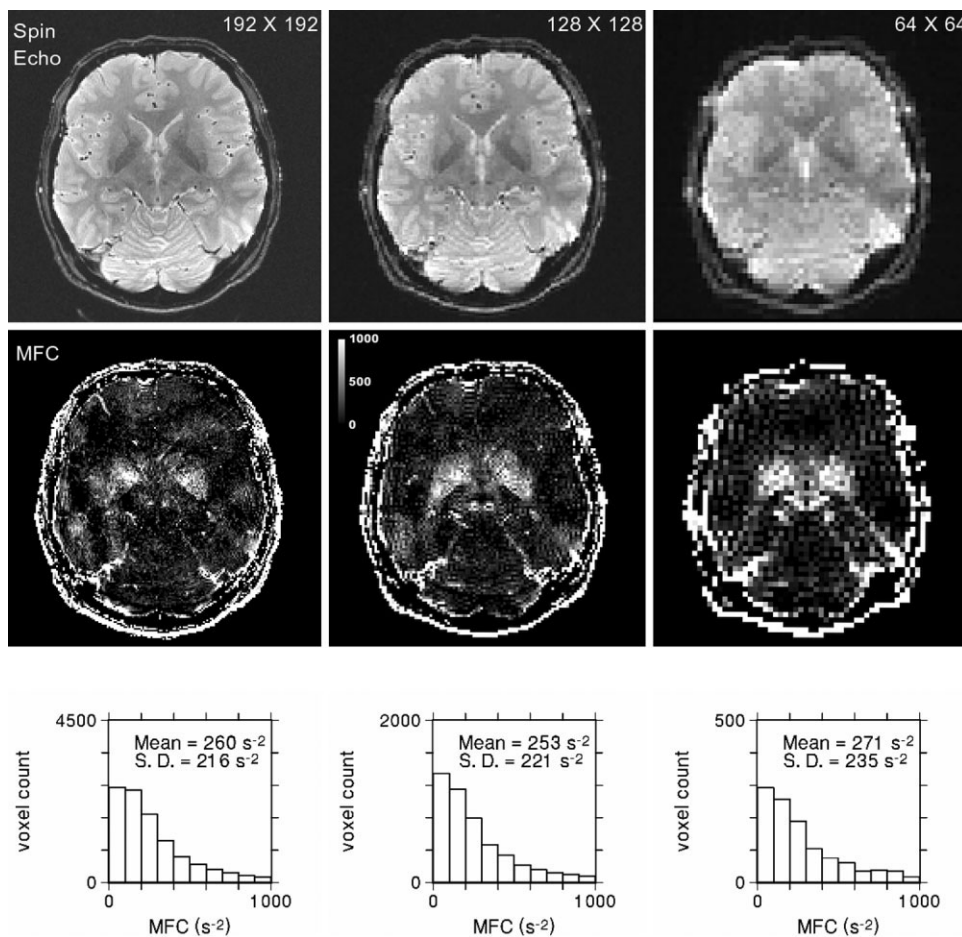


FIG. 7. SSE images and MFC maps acquired with  $TE = 42$  ms for three different resolutions at similar anatomical locations. Also shown are the corresponding MFC histograms for voxels with MFC values  $>0$  and  $<1000 \text{ s}^{-2}$ . Macroscopic gradients in the image plane give a contribution to the MFC that increases quadratically with the voxel dimensions, as follows from Eq. [27]. The similarity of the three histograms suggests that macroscopic in-plane gradients have a minor effect on the MFC values in this case. Note that the ordinates of the histograms have been scaled as the inverse of the voxel volume so that the lengths of the bars are directly comparable (the slice thickness is 1.1 mm for all three resolutions).

termed gradient-echo sampling of free induction decay and echo (GESFIDE), is also based on ASE acquisitions, but differs in three important aspects. First, the position of the  $180^\circ$  refocusing pulse is fixed, but the image acquisition time is varied. Second, the data is fit to monoexponential signal decay forms. Third, the method yields estimates for  $R_2$ ,  $R_2^*$ , and  $R_2'$ , rather than for the MFC. A possible limitation of this method is that significant deviations from monoexponential decay have been observed in both blood (16) and bone (18).

In prior work, we have reported numerical evidence obtained with Monte Carlo simulations (19) and experimental evidence for yeast cell suspensions (20) to support the validity and feasibility of MFC imaging, and an initial human MFC image was presented in Ref. 21. The phantom results given here confirm and extend the conclusions obtained with yeast cell suspensions. The close agreement between the theoretical form of Eq. [30] and the data shown in Fig. 2 attests to the accuracy, in this case, of a Gaussian fit. The predicted decrease of the MFC with time is clearly demonstrated by the data of Fig. 3. The fit of this data to Eq. [33], with reasonable values for the fitting parameters, also supports the underlying theory of MFC imaging. In particular, the phantom data confirms that the measured MFC values scale with the applied field as predicted theoretically.

Our human results are consistent with those of the phantom study, with a good fit to Eq. [30] observed in the putamen, but with some indication of a deviation from Gaussian behavior for shifts  $|t_s| \geq 16$  ms. While a decrease of the MFC with increasing time is observed, it is not statistically significant. A high MFC is found in both the putamen and the globus pallidus, which is likely due to the known high iron concentration of these regions (34). A high MFC is also seen in other brain areas, such as near large blood veins. The MFC maps of Fig. 4 are distinguished from the corresponding  $R_2$  maps because they have a much larger contrast between the basal ganglia structures and the surrounding tissue. This suggests the possibility that MFC imaging may provide a more sensitive method of brain iron quantification than the use of  $R_2$  maps.

An important issue is the length scale of the MFIs that contribute to the MFC values observed in the brain parenchyma. The results shown in Fig. 7 indicate at most a small contribution from macroscopic gradients parallel to the image plane, although this result may depend on the slice selection and orientation. The decrease in the MFC with time in the putamen points to a significant contribution from microscopic MFIs with a length scale on the order of micrometers. However, additional investigation of the origin of the MFIs is warranted. It should nonetheless be emphasized that any contribution of macroscopic gradients can be strongly suppressed by reducing the voxel dimensions.

The MFC maps of Figs. 4 and 7 show a significant amount intraregional MFC heterogeneity within the putamen and other brain regions. This may reflect spatial inhomogeneities in nonheme brain iron, and indeed Haacke et al. (39) have reported qualitatively similar results in the basal ganglia with susceptibility-weighted imaging. Alternatively, blood veins, motion artifacts, and noise could be

contributing factors. It may be noted that some spatial inhomogeneity is also apparent in the phantom MFC map of Fig. 1, which is likely due, at least in part, to imaging artifacts rather than true MFC variations.

As discussed, the MFC is affected by water diffusion, as well as the MFIs. Therefore, it can be helpful to acquire diffusion-weighted MRI data in conjunction with MFC measurements in order to better interpret MFC differences. This may be particularly important for tumors and tissues with edema. In normal brain, however, diffusion coefficients are fairly uniform within the brain parenchyma, and so regional variations in water diffusion are unlikely to alter MFC contrast significantly. As demonstrated with our phantom study, the effects of water diffusion and the MFIs can potentially be separated by measuring the MFC at several different times and fitting to a model, such as the one given by Eq. [33].

Further experimental validation and development of MFC imaging is needed to demonstrate practical advantages over conventional relaxations rates for the quantification of tissue properties, such as iron concentration. Most importantly, the connection between MFC and brain iron should be investigated in greater detail both with animal studies, which would allow for a direct comparison to histological iron measures, and with more human studies. In addition, the effect of imaging artifacts, such as EPI-related ghosting, motion, and vascular pulsation, should be explored. Finally, the confounding effect of macroscopic MFIs should be evaluated more thoroughly; the explicit decomposition of the MFC into microscopic and macroscopic components given by Eq. [27] hints at a refined MFC imaging method that would allow these to be measured independently.

Because the MFC grows approximately with the square of the applied field strength, high field scanners are especially suitable for MFC imaging. It should nevertheless be remembered that the main theoretical basis for MFC imaging relies on a weak field approximation, and Eqs. [8] and [10] may become inaccurate if the field level is too high (19).

The quadratic dependence of the MFC on the applied field also suggests that the "rescaled MFC"  $\equiv \text{MFC}/B_0^2$  may be regarded an intrinsic tissue property. However, the previously noted weak nonlinearities in magnetic characteristics of ferritin iron (23) imply that this rescaled MFC can, in fact, have a residual field dependence. An additional dependence on the relative orientation of a tissue to the direction of the applied field can occur both because of macroscopic gradients, which may change with body alignment, and anisotropic tissue properties (as in white matter).

Because iron compounds, such as ferritin and hemosiderin, are the most commonly occurring paramagnetic substances within the human body, iron quantification is a potential application of MFC imaging. Additional tissue properties could be studied by administering a paramagnetic contrast agent, for example Gd-DTPA. Since these agents remain in the extracellular spaces, they can generate significant microscopic MFIs. It is then at least conceivable that MFC imaging may be able to yield information about the cellular morphology of pathological tissues, including tumors.

## CONCLUSION

We have shown how a new physical quantity, the MFC, can, in principle, be measured in vivo by means of MRI. The key to MFC imaging is the fitting of ASE data to Eq. [8] (or Eq. [30]). Since MFC images are prone to motion artifacts, an EPI acquisition and image coregistration were utilized for the preliminary MFC maps shown here. In addition, voxels with small dimensions were employed to reduce the effects of macroscopic gradients. While the data presented supports the feasibility of MFC imaging, considerable work remains in the validation and optimization of this technique.

## APPENDIX

### Derivation of Eq. [6]

From Eq. [5], it is straightforward to demonstrate

$$\begin{aligned} \ln \left[ \frac{S(t; t/2)}{S(t; t_s + t/2)} \right] &= \frac{\gamma^2}{2} \int_0^{t_s+t/2} dt_a \int_0^{t_s+t/2} dt_b K(|t_a - t_b|) \\ &\quad - \frac{\gamma^2}{2} \int_0^{t/2} dt_a \int_0^{t/2} dt_b K(|t_a - t_b|) - \gamma^2 \int_{t_s+t/2}^t dt_a \int_0^{t_s+t/2} dt_b K(|t_a - t_b|) \\ &\quad + \gamma^2 \int_{t/2}^t dt_a \int_0^{t/2} dt_b K(|t_a - t_b|) + \frac{\gamma^2}{2} \int_{t_s+t/2}^t dt_a \int_{t_s+t/2}^t dt_b K(|t_a - t_b|) \\ &\quad - \frac{\gamma^2}{2} \int_{t/2}^t dt_a \int_{t/2}^t dt_b K(|t_a - t_b|), \quad [A1] \end{aligned}$$

where  $t_s$  is the shift of  $t_p$  from the SSE value of  $t/2$ .

A rearrangement of the integrals in Eq. [A1] results in

$$\begin{aligned} \ln \left[ \frac{S(t; t/2)}{S(t; t_s + t/2)} \right] &= 2\gamma^2 \int_{t/2}^{t_s+t/2} dt_a \int_0^{t/2} dt_b K(|t_a - t_b|) \\ &\quad - 2\gamma^2 \int_{t_s+t/2}^t dt_a \int_{t/2}^{t_s+t/2} dt_b K(|t_a - t_b|). \quad [A2] \end{aligned}$$

With the change of variables  $t_a \rightarrow t - t_b$  and  $t_b \rightarrow t - t_a$  in the second integral on the right hand side of Eq. [A2], we find

$$\begin{aligned} \ln \left[ \frac{S(t; t/2)}{S(t; t_s + t/2)} \right] &= 2\gamma^2 \int_{t/2}^{t_s+t/2} dt_a \int_0^{t/2} dt_b K(|t_a - t_b|) \\ &\quad - 2\gamma^2 \int_{-t_s+t/2}^{t/2} dt_a \int_0^{-t_s+t/2} dt_b K(|t_a - t_b|). \quad [A3] \end{aligned}$$

A second change of variables in the second integral,  $t_a \rightarrow t_a - t_s$  and  $t_b \rightarrow t_b - t_s$ , gives

$$\begin{aligned} \ln \left[ \frac{S(t; t/2)}{S(t; t_s + t/2)} \right] &= 2\gamma^2 \int_{t/2}^{t_s+t/2} dt_a \int_0^{t/2} dt_b K(|t_a - t_b|) \\ &\quad - 2\gamma^2 \int_{t/2}^{t_s+t/2} dt_a \int_{t_s}^{t/2} dt_b K(|t_a - t_b|). \quad [A4] \end{aligned}$$

By combining the two right hand side terms and making the transformation  $t_a \rightarrow t_a + t/2$ , one then sees that

$$\ln \left[ \frac{S(t; t/2)}{S(t; t_s + t/2)} \right] = 2\gamma^2 \int_0^{t_s} dt_a \int_0^{t_s} dt_b K(t_a - t_b + t/2). \quad [A5]$$

A final variable change of  $t_a - t_b \rightarrow s$  and  $(t_a + t_b)/2 \rightarrow u$  allows the integral over  $u$  to be performed explicitly, leading directly to the result of Eq. [6].

### Derivation of Eq. [26]

Note that Schwarz's inequality gives

$$|\langle [B_{\text{micro}}(t) - B_{\text{micro}}(t')] \{ \mathbf{G} \cdot [\mathbf{r}(t) - \mathbf{r}(t')] \} \rangle| \leq \langle [B_{\text{micro}}(t) - B_{\text{micro}}(t')]^2 \rangle^{1/2} \times \langle \{ \mathbf{G} \cdot [\mathbf{r}(t) - \mathbf{r}(t')] \}^2 \rangle^{1/2}. \quad [A6]$$

From time translation invariance, it can be deduced that

$$\begin{aligned} \langle [B_{\text{micro}}(t) - B_{\text{micro}}(t')]^2 \rangle &= 2\langle [B_{\text{micro}}(0)]^2 \rangle - 2\langle B_{\text{micro}}(t) B_{\text{micro}}(t') \rangle \\ &\leq 2\langle [B_{\text{micro}}(0)]^2 \rangle \equiv 2K_{\text{micro}}(0), \quad [A7] \end{aligned}$$

where it has been assumed that  $K_{\text{micro}}(t) \geq 0$ . From Eqs. [A6] and [A7], one then sees that

$$\begin{aligned} |\langle [B_{\text{micro}}(t) - B_{\text{micro}}(t')] \{ \mathbf{G} \cdot [\mathbf{r}(t) - \mathbf{r}(t')] \} \rangle| &\leq [2K_{\text{micro}}(0)]^{1/2} \\ &\times \langle \{ \mathbf{G} \cdot [\mathbf{r}(t) - \mathbf{r}(t')] \}^2 \rangle^{1/2}. \quad [A8] \end{aligned}$$

As previously discussed in the Theory section, for a practical MRI experiment

$$\langle \{ \mathbf{G} \cdot [\mathbf{r}(t) - \mathbf{r}(t')] \}^2 \rangle < \frac{1}{6} (G_x^2 L_x^2 + G_y^2 L_y^2 + G_z^2 L_z^2). \quad [A9]$$

Applying this result together with the algebraic inequality  $x^2 + y^2 \geq 2xy$  to Eq. [A8] then yields

$$\begin{aligned} |\langle [B_{\text{micro}}(t) - B_{\text{micro}}(t')] \{ \mathbf{G} \cdot [\mathbf{r}(t) - \mathbf{r}(t')] \} \rangle| &\ll K_{\text{micro}}(0) \\ &+ \frac{1}{12} (G_x^2 L_x^2 + G_y^2 L_y^2 + G_z^2 L_z^2), \quad [A10] \end{aligned}$$

from which Eq. [26] follows.

## ACKNOWLEDGMENTS

This work was supported in part by grants from the National Institutes of Health (NIH/NIBIB R21/R33 EB003305 to J.H.J) and from the Institute for the Study of Aging and the Werner Dannheisser Testamentary Trust (to J.A.H.).

## REFERENCES

1. Schenck JF, Zimmerman EA. High-field magnetic resonance imaging of brain iron: birth of a biomarker? *NMR Biomed* 2004;17:433–445.
2. St Pierre TG, Clark PR, Chua-Anusorn W. Single spin-echo proton transverse relaxometry of iron-loaded liver. *NMR Biomed* 2004;17:446–458.
3. St Pierre TG, Clark PR, Chua-anusorn W, Fleming AJ, Jeffrey GP, Olynyk JK, Pootrakul P, Robins E, Lindeman R. Noninvasive measurement and imaging of liver iron concentrations using proton magnetic resonance. *Blood* 2005;105:855–861.
4. Westwood M, Anderson LJ, Firmin DN, Gatehouse PD, Charrier CC, Wonke B, Pennell DJ. A single breath-hold multiecho  $T_2^*$  cardiovascular magnetic resonance technique for diagnosis of myocardial iron overload. *J Magn Reson Imaging* 2003;18:33–39.
5. Wood JC, Tyszka JM, Carson S, Nelson MD, Coates TD. Myocardial iron loading in transfusion-dependent thalassemia and sickle cell disease. *Blood* 2004;103:1934–1936.
6. Ordridge RJ, Gorell JM, Deniau JC, Knight RA, Helpert JA. Assessment of relative brain iron concentrations using  $T_2$ -weighted and  $T_2^*$ -weighted MRI at 3 Tesla. *Magn Reson Med* 1994;32:335–341.
7. Ma J, Wehrli FW. Method for image-based measurement of the reversible and irreversible contribution to the transverse-relaxation rate. *J Magn Reson B* 1996;111:61–69.
8. Gelman N, Gorell JM, Barker PB, Savage RM, Spickler EM, Windham JP, Knight RA. MR imaging of human brain at 3.0 T: preliminary report on transverse relaxation rates and relation to estimated iron content. *Radiology* 1999;210:759–767.
9. Yablonskiy DA, Haacke EM. Theory of NMR signal behavior in magnetically inhomogeneous tissues: the static dephasing regime. *Magn Reson Med* 1994;32:749–763.
10. Kiselev VG, Posse S. Analytical theory of susceptibility induced NMR signal dephasing in a cerebrovascular network. *Phys Rev Lett* 1998;81:5696–5699.
11. Kiselev VG, Posse S. Analytical model of susceptibility-induced MR signal dephasing: effect of diffusion in a microvascular network. *Magn Reson Med* 1999;41:499–509.
12. Jensen JH, Chandra R. Strong field behavior of the NMR signal from magnetically heterogeneous tissues. *Magn Reson Med* 2000;43:226–236.
13. Jensen JH, Chandra R. NMR relaxation in tissues with weak magnetic inhomogeneities. *Magn Reson Med* 2000;44:144–156.
14. Sukstanskii AL, Yablonskiy DA. Theory of FID NMR signal dephasing induced by mesoscopic magnetic field inhomogeneities in biological systems. *J Magn Reson* 2001;151:107–117.
15. Sukstanskii AL, Yablonskiy DA. Gaussian approximation in the theory of MR signal formation in the presence of structure-specific magnetic field inhomogeneities. *J Magn Reson* 2003;163:236–247.
16. Spees WM, Yablonskiy DA, Oswood MC, Ackerman JJH. Water proton MR properties of human blood at 1.5 Tesla: magnetic susceptibility,  $T_1$ ,  $T_2$ ,  $T_2^*$ , and non-Lorentzian signal behavior. *Magn Reson Med* 2001;45:533–542.
17. Jensen JH, Chandra R. Theory of nonexponential NMR signal decay in liver with iron overload or superparamagnetic iron oxide particles. *Magn Reson Med* 2002;47:1131–1138.
18. Newitt DC, Majumdar S, Jergas MD, Genant HK. Decay characteristics of bone marrow in the presence of a trabecular bone network: in vitro and in vivo studies showing a departure from monoexponential behavior. *Magn Reson Med* 1996;35:921–927.
19. Jensen JH, Chandra R. Method for measuring the magnetic field correlation function for water protons in biological tissues. In: *Proceedings of the 10th Annual Meeting of ISMRM, Honolulu, HI, USA, 2002*. p. 2297.
20. Jensen JH, Johnson G, Chandra R, Helpert JA. MRI measurement of magnetic field correlation in a cell suspension. In: *Proceedings of the 11th Annual Meeting of ISMRM, Toronto, Ontario, Canada, 2003*. p. 1120.
21. Helpert JA, Jensen J, Lee SP, Falangola MF. Quantitative MRI assessment of Alzheimer's disease. *J Mol Neurosci* 2004;24:45–48.
22. Piñero DJ, Connor JR. Iron in the brain: an important contributor in normal and diseased states. *Neuroscientist* 2000;6:435–453.
23. Brooks RA, Vymazal J, Goldfarb RB, Bulte JW, Aisen P. Relaxometry and magnetometry of ferritin. *Magn Reson Med* 1998;40:227–235.
24. Dixon WT. Simple proton spectroscopic imaging. *Radiology* 1984;153:189–194.
25. Kennan RP, Zhong J, Gore JC. Intravascular susceptibility contrast mechanisms in tissues. *Magn Reson Med* 1994;31:9–21.
26. Brooks RA, Vymazal J, Bulte JWM, Baumgarner CD, Tran V. Comparison of  $T_2$  relaxation in blood, brain, and ferritin. *J Magn Reson Imag* 1995;4:446–450.
27. Ye FQ, Allen PS. Relaxation enhancement of the transverse magnetization of water protons in paramagnetic suspensions of red blood cells. *Magn Reson Med* 1995;34:713–720.
28. Vymazal J, Brooks RA, Baumgarner C, Tran V, Katz D, Bulte JWM, Bauminger ER, Di Chiro G. The relation between brain iron and NMR relaxation times: an in vitro study. *Magn Reson Med* 1996;35:56–61.
29. Ye FQ, Martin WRW, Allen PS. Estimation of the iron concentration in excised gray matter by means of proton relaxation measurements. *Magn Reson Med* 1996;35:285–289.
30. Jensen JH, Chandra R, Yu H. Quantitative model for the interecho time dependence of the CPMG relaxation rate in iron-rich gray matter. *Magn Reson Med* 2001;46:159–165.
31. Press WH, Teukolsky SA, Vetterling WT, Flannery BP. *Numerical recipes in C: the art of scientific computing*. New York: Cambridge University Press; 1992.
32. Henkelman RM. Measurement of signal intensities in the presence of noise in MR images. *Med Phys* 1985;232–233.
33. Kuznetsov OA, Brown CS, Levine HG, Piasuch WC, Sanwo-Lewandowski MM, Hasenstein KH. Composition and physical properties of starch in microgravity-grown plants. *Adv Space Res* 2001;28:651–658.
34. Hallgren B, Sourander P. The effect of age on the non-haemin iron in the human brain. *J Neurochem* 1958;3:41–51.
35. Wismer GL, Buxton RB, Rosen BR, Fisel CR, Oot RF, Brady TJ, Davis KR. Susceptibility induced MR line broadening: applications to brain iron mapping. *J Comput Assist Tomography* 1988;12:259–265.
36. Hoppel BE, Weisskoff RM, Thulborn KR, Moore JB, Kwong KK, Rosen BR. Measurement of regional blood oxygenation and cerebral hemodynamics. *Magn Reson Med* 1993;30:715–723.
37. Ganesan K, Ailon DC, Cuttillo AG, Goodrich KC. New technique for obtaining NMR linewidth images of lung and other inhomogeneously broadened systems. *J Magn Reson B* 1993;102:293–298.
38. Stables LA, Kennan RP, Gore JC. Asymmetric spin echo imaging of magnetically inhomogeneous systems: theory, experiment, and numerical studies. *Magn Reson Med* 1998;40:432–442.
39. Haacke EM, Xu Y, Cheng YC, Reichenbach JR. Susceptibility weighted imaging (SWI). *Magn Reson Med* 2004;52:612–618.